



Effect of cobalt doping-regulated crystallinity in nickel-iron layered double hydroxide catalyzing oxygen evolution

Yang Yang^a, Shuya Wei^b, Yafei Li^{b,*}, Donggang Guo^{c,*}, Huajie Liu^{d,*}, Lu Liu^{a,*}

^a Tianjin Key Laboratory of Environmental Remediation and Pollution Control, College of Environmental Science and Engineering, Nankai University, Tianjin 300350, China

^b Jiangsu Key Laboratory of New Power Batteries, Jiangsu Collaborative Innovation Centre of Biomedical Functional Materials, School of Chemistry and Materials Science, Nanjing Normal University, Nanjing 210023, China

^c Shanxi Laboratory for Yellow River, College of Environment and Resource, Shanxi University, 92 Wucheng Rd., Shanxi 030006, China

^d School of Chemical Science and Engineering, Shanghai Research Institute for Intelligent Autonomous Systems, Key Laboratory of Advanced Civil Engineering Materials of Ministry of Education, Tongji University, Shanghai 200092, China

ARTICLE INFO

Keywords:

NiFe layered double hydroxides
Crystalline-amorphous heterostructures
Electrocatalysis
Oxygen evolution reaction
Ultrathin nanosheets

ABSTRACT

The formation of a crystalline-amorphous (c-a) interface by modulating the crystallinity of the material is a promising strategy for oxygen evolution reaction (OER). Therefore, a similar element substitution approach is reported in this study to regulate the catalyst's crystallinity. Adjustment of the cobalt content in NiFe layered double hydroxide (LDH) by the solvothermal method enables the control of c-a interfacial site of the material. In 1 M KOH, the as-obtained Co_{1.98}-NiFe LDH exhibited a low overpotential of 236 mV to achieve 20 mA cm⁻². It also showed excellent stability, operating steadily at high current densities for 96 h without significant degradation in 1 M KOH or alkaline artificial and natural seawater electrolytes. Therefore, the OER activity of the catalysts was improved while ensuring structural stability. We believe that this method will provide new insights and perspectives for the development of highly efficient and stable OER catalysts.

1. Introduction

Water splitting has attracted significant attention for producing hydrogen, a green and clean energy source, owing to the increasing energy demand and severe environmental problems [1–3]. Water splitting occurs through two basic half-reactions, i.e., hydrogen evolution reaction (HER) at the cathode and oxygen evolution reaction (OER) at the anode. However, owing to the complex four-electron process and slow kinetics of the OER with a large overpotential, large-scale hydrogen production by water splitting requires a high amount of energy [4–6]. Noble metal oxides, such as IrO₂ and RuO₂, are currently used as representative electrocatalysts for OER [7,8]. However, their applications are limited to a small scale due to their high cost, low quantity, and low stability under operating conditions [9,10]. Therefore, several studies have focused on using low-cost and abundant transition metals as alternative materials [11–14].

To date, various earth-abundant materials, predominantly two-dimensional (2D) LDHs based on the first row of transition metal elements (including Ni, Co, and Fe), have proven to be promising OER catalysts [15–18]. In 2D materials, the primary active sites are edge sites and defects, and their close-packed basal planes severely limit the exposure of the active sites. Therefore, activating and fabricating internal functional areas is promising for improving electrocatalytic activity [19,20]. The manufacturing of the crystalline-amorphous (c-a) heterostructure has been proven to be a progressive OER catalyst design that incorporates the high electrical conductivity of the crystalline phase and the rich unsaturated sites of the amorphous phase [21–23]. In addition, the c-a interface can regulate the electron density of interfacial sites to optimize the adsorption/desorption of O-containing intermediates and improve the charge-transfer process during the OER process [24–26]. However, it is difficult to achieve highly dense c-a interfacial sites by most synthetic methods and the amorphous phase is

Abbreviations: HER, hydrogen evolution reaction; OER, oxygen evolution reaction; LDH, layered double hydroxide; XRD, X-ray diffraction; LSV, linear sweep voltammetry; CV, cyclic voltammetry; RHE, reversible hydrogen electrode; TEM, transmission electron microscopy; XPS, X-ray photoelectron spectroscopy; EIS, electrochemical impedance spectroscopy; ECSA, electrochemically effective surface area; LOM, lattice-oxygen-mediated mechanism.

* Corresponding authors.

E-mail addresses: liyafei@njnu.edu.cn (Y. Li), gdghjx@126.com (D. Guo), liuhujie@tongji.edu.cn (H. Liu), liul@nankai.edu.cn (L. Liu).

<https://doi.org/10.1016/j.apcatb.2022.121491>

Received 15 February 2022; Received in revised form 29 April 2022; Accepted 6 May 2022

Available online 10 May 2022

0926-3373/© 2022 Elsevier B.V. All rights reserved.

achieved by introducing other heteroatoms to disrupt the crystal structure [27–29]. Although they are inherently rich in defects acting as active sites, amorphous interfaces also result in poor stabilities. Moreover, its low electrical conductivity severely limits the charge-transfer kinetics [30]. Therefore, it is crucial to balance the amorphous and crystalline phases of the material for the rational design of applicable OER electrocatalysts.

A straightforward solvothermal method was used to select NiFe layered double hydroxide (NiFe LDH) as the structure substrate and was doped with cobalt. Because Co and Ni have similar atomic structures and physicochemical properties, the Co atom can gradually replace the Ni atom in the crystal structure, from unsaturated to saturated states. The inherent crystallinity of the substance is controlled to realize a stable crystal structure and maximize the formation of the c-a interface. Moreover, the presence of high-valent Co ions contributed to improving the inherent activity of the as-obtained catalysts. The final synthesized Co-NiFe LDH material exhibited both excellent activity and outstanding stability. The Co_{1.98}-NiFe LDH catalyst displays outstanding performance when employed directly as an OER electrode in the following electrolytes: 1.0 M KOH (236 mV at 20 mA cm⁻²), 1.0 M KOH + 0.5 M NaCl (254 mV at 20 mA cm⁻²), 1.0 M KOH + 1.0 M NaCl (255 mV at 20 mA cm⁻²), and 1.0 M KOH + seawater (261 mV at 20 mA cm⁻²). A highly efficient two-electrode electrolyzer was fabricated by coupling this OER catalyst with an advanced Pt/C (20 wt%) HER catalyst. A current density of 10 mA cm⁻² at a low voltage of 1.5 V (1.53 V in 1.0 M KOH + seawater) indicated good durability with no significant decay over 96 h. Using similar elements for doping to regulate the crystallinity of the material provides a new perspective for further development of more efficient and robust OER catalysts.

2. Experimental section

2.1. Chemicals and reagents

Iron (III) nitrate nonahydrate (Fe(NO₃)₃·9H₂O, ≥ 98.5%), cobalt(II) nitrate hexahydrate (Co(NO₃)₂·6H₂O, ≥ 99%), nickel (II) nitrate hexahydrate (Ni(NO₃)₂·6H₂O, ≥ 98%), urea (≥ 99%), and ammonium fluoride (NH₄F, ≥ 96%) were purchased from Shanghai Macklin Biochemical Co., Ltd. Ruthenium oxide hydrate (RuO₂, metal basis) and potassium hydroxide (KOH, ≥ 95%) were purchased from Shanghai Aladdin Biochemical Technology Co., Ltd. The Nafion dispersion (5 wt %) and commercial Pt/C (20 wt%) were purchased from Alfa Aesar. N, N-Dimethylformamide (DMF, ≥ 99.5%) and ethylene glycol (≥ 99.7%) were purchased from Tianjin Fengchuan Chemical Technology Co., Ltd. Carbon fiber paper (TGP-H-090) was purchased from the Fuel Cell Store. All reaction reagents and chemicals were obtained and used in their as-received form without further purification.

2.2. Synthesized progress

The overall synthesis process was a simple solvothermal reaction. First, Co(NO₃)₂·6H₂O, 0.25 mmol Fe(NO₃)₃·9H₂O, 0.5 mmol Ni(NO₃)₂·6H₂O, 2.5 mmol urea, and 2 mmol NH₄F were dissolved in a solution consisting of 25 mL ethylene glycol and 10 mL DMF. The amount of Co(NO₃)₂·6H₂O added, which was varied for obtaining different samples, was 0, 0.025, 0.125, 0.165, 0.245, 0.285, and 0.325 mmol. After thorough stirring and dissolution, the prepared homogeneous solution was loaded into a PTFE reactor and heated at 140 °C for 12 h. After cooling to room temperature (~ 24 °C), the products were washed more than five times with water and ethanol to remove any impurities. Finally, the samples were vacuum dried overnight at 60 °C.

2.3. Material characterizations

The morphologies and dimensions of the materials were measured using field-emission scanning electron microscopy (FESEM, JSM-7800

F). The crystal structure and purity of the products were determined by powder X-ray diffraction (XRD, D/max-2500, JAPAN SCIENCE) with Cu Kα radiation (λ = 1.5418 Å) in the 2θ range of 5–80°. The crystallinities of the materials were obtained from the XRD spectra according to the following equation:

$$\text{Crystallinity}(\%) = \frac{\text{Area of crystalline peaks}}{\text{Area of all peaks}(\text{crystalline} + \text{amorphous})} \times 100\%.$$

Transmission electron images, high-resolution transmission electron microscopy images, and elemental profiles were acquired using high-resolution field-emission transmission electron microscopy (TEM) (Tecnai G2 F20, FEI) with energy dispersive X-ray and STEM attachments. To analyze the surface chemistry of the products and to verify the composition of the products, X-ray photoelectron spectroscopy (XPS) analysis was performed on a Thermo Scientific ESCALAB 250Xi instrument (Thermo, USA). The metal concentration was determined using a continuous light atomic absorption spectrometer (AAS, contraAA 700, Germany) on an air acetylene flame. Operando Raman spectra were recorded using a Renishaw inVia Evolution Raman spectrometer with an excitation wavelength of 532 nm under a controlled potential. The gas products from the electrolysis were detected to the gas chromatograph (Shimadzu, GC 2014c).

2.4. Electrochemical measurements

The catalyst ink suspensions were prepared by diluting the sample powders in deionized water, ethanol, and a Nafion solution mixture. The catalyst powder (5 mg) was dispersed in a solution of deionized water (480 μL) and ethyl alcohol (500 μL) with 20 μL of 5 wt% Nafion solution by sonicating for 1 h to disperse the catalyst power, and the Nafion ionomer (RuO₂ and Pt/C were prepared in the same way). Then, 200 μL of the ink was drop-casted on a piece of carbon fiber paper at 1 cm⁻² (loading 1 mg cm⁻²) and dried at room temperature.

Electrochemical tests were performed on a Zennium electrochemical workstation (Zahner, Germany) in a standard three-electrode system at room temperature. A carbon rod, Hg/HgO electrode, and samples were employed as the counter, reference, and working electrodes, respectively. Herein, 1 M KOH, 0.5 M NaCl + 1 M KOH, 1 M NaCl + 1 M KOH (pH = 13.8), and nature seawater + 1 M KOH (pH = 13.6) were passed through for 30 min to saturate them with oxygen before using as electrolytes during the electrocatalytic test. Natural seawater was obtained from Dongjiang Bay (Tianjin, China). The natural seawater + 1 M KOH solution was prepared by directly replacing the solvent deionized water with natural seawater to make a 1 M KOH solution and then removing the precipitate to be used as an electrolyte.

First, the samples were subjected to cyclic voltammetry (CV) for at least 400 cycles to reach a steady state before routine testing. Linear sweep voltammetry (LSV) was performed at a scan rate of 5 mV s⁻¹ in the range 0.912–1.912 V (vs. reversible hydrogen electrode (RHE)). The iR-drop correction was applied to all the polarization curves. The Tafel slope was inferred from $\eta = a + b \times \log j$, where a is a constant and b refers to the Tafel slope. The current density, j , was normalized to the geometrical area. Electrochemical impedance spectral data were obtained at an overpotential of 300 mV with an AC amplitude of 10 mV applied in the frequency range of 10⁻¹–10⁵ Hz. The electrochemical impedance spectroscopy (EIS) data were fitted using Zman software. The CV curves were obtained at scan rates ranging from 20 to 45 mV s⁻¹ and potential from 0.05 to 0.15 V (vs. Hg/HgO) to calculate the double-layer capacity (C_{dl}). The C_{dl} was further converted into the electrochemical active surface area (ECSA) using the specific capacitance value for a standard with 1 cm² of actual surface area. The ECSA of each catalyst was calculated using the expression $A_{ECSA} = C_{dl}/C_s$. The specific capacitance in 1 M KOH was 0.040 mF cm⁻². The turnover frequency (TOF) values were calculated as follows:

$$\text{TOF} = j/4nF,$$

where j is the current density at an overpotential of 300 mV during the LSV measurement in 1.0 M KOH, F is the Faradaic constant (96485 C mol^{-1}), and n is the number of active sites. All the metal ions were assumed as active sites, as established by AAS. The stability of the samples was measured by chronopotentiometry at a current density of 100 mA cm^{-2} for an extended period.

The overall water splitting was performed in a two-electrode system, in which $\text{Co}_{1.98}\text{-NiFe LDH}$ served as the positive electrode for the OER and Pt/C (20 wt%) acted as the negative electrode for the HER. The catalytic durability of the two-electrode cell system for overall water splitting was measured using different electrolytes at fixed current density of 10 mA cm^{-2} . The potentials obtained were adjusted using a RHE ($E_{\text{RHE}} = E_{\text{Hg/HgO}} + 0.098 + 0.059 \times \text{pH}$). The iR -corrected potential ($E_{iR\text{-free}}$) was determined from the experimentally measured EIS solution resistance (R_s) using the equation:

$$E_{iR\text{-free}} = E - iR_s.$$

The overpotential (η) was calculated according to the equation:

$$\eta = E_{iR\text{-free}} - 1.23 \text{ V}.$$

2.5. In-situ Raman spectroscopy

All in-situ Raman spectroscopy experiments were performed using a Raman spectrometer (inVia confocal Raman microscope, Renishaw) equipped with an in-situ test electrolyte cell (Gaoss Union C031-2). The laser excitation wavelength was 532 nm. The Raman shift range was calibrated using a peak of $520 \pm 0.5 \text{ cm}^{-1}$ in silicon before the measurements. Each in-situ spectrum was recorded by accumulating 40 scans at a resolution of 1 cm^{-1} . The exposure time for each spectrum was 30 min. The working electrodes used in this study were the same as those used in the electrocatalytic OER tests. The working electrodes were assembled using a custom electrochemical cell for the subsequent in-situ Raman spectroscopy measurements. A fixed potential was applied for a specific time in a typical test procedure, and the Raman spectra were recorded at different potentials (open circuit potential (OCP)–1.8 V vs. RHE).

2.6. DFT calculation

The Vienna ab initio simulation package was used to performed the

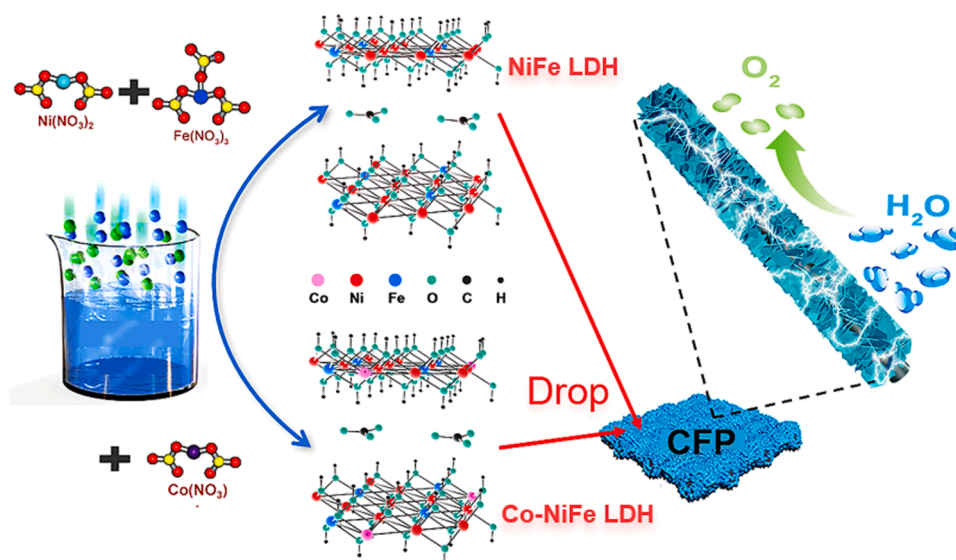
density functional theory calculations. The exchange-correlation energy was modeled by the generalized gradient approximation using Perdew-Burke-Ernzerh of functional. The kinetic energy cutoff of the plan-wave basis set was 400 eV and a $1 \times 1 \times 1$ k-point mesh was chosen to sample the Brillouin zone in the structural optimizations. The supercell was separated by a 35 Å vacuum along the z-axis to prevent adjacent periodic units. The energy and force convergence thresholds for the iteration in the self-consistent field were set to $5 \times 10^{-5} \text{ eV}$ and 0.05 eV/Å , respectively.

3. Results and discussion

3.1. Synthesis and characterizations of catalysts

Both pristine NiFe and Co-NiFe LDH were synthesized using a one-step solvothermal method, but different cobalt precursors were added (Scheme 1). The complete process and parameters used are detailed in the Experimental Procedure section of the supporting materials. The Co/Ni/Fe ratios of the samples were adjusted and determined using flame atomic absorption spectroscopy (Table S1-S2). They were labeled as NiFe LDH, $\text{Co}_{0.55}\text{-NiFe LDH}$, $\text{Co}_{1.50}\text{-NiFe LDH}$, $\text{Co}_{1.88}\text{-NiFe LDH}$, $\text{Co}_{1.98}\text{-NiFe LDH}$, $\text{Co}_{2.20}\text{-NiFe LDH}$, and $\text{Co}_{2.48}\text{-NiFe LDH}$.

XRD was used to analyze the material composition and crystal structure of the as-prepared samples. The NiFe LDH exhibited a typical $\text{Ni}_6\text{Fe}_2(\text{CO}_3)(\text{OH})_{16}$ (PDF#26-1286) phase structure, and a series of Co-NiFe LDH samples also showed a similar pattern (Fig. 1a). When the crystallinity of the samples was calculated, it revealed an oscillatory pattern as the Co content increased (Fig. 1b). The morphology of all samples was examined using scanning electron microscopy (SEM) to evaluate the impact of elemental cobalt on the morphology. As shown in Fig. S1-S2 and Fig. 1c, both the doped samples and the original NiFe LDH showed tiny nanosheet morphologies, indicating that Co doping did not significantly affect the sample morphology. TEM was used to investigate the microstructures of the samples. Both the samples exhibited ultrathin nanosheet structures, as shown in Fig. 1d and Fig. S3b-d. In addition, atomic force microscopy demonstrated the ultrathin nanosheet features of $\text{Co}_{1.98}\text{-NiFe LDH}$ with a thickness of approximately 4.0 nm (Fig. S4). High-resolution TEM showed a lattice spacing of 0.26 nm corresponding to the (204) crystal plane of $\text{Ni}_6\text{Fe}_2(\text{CO}_3)(\text{OH})_{16}$, which is consistent with the above XRD results. This indicates that the sample comprised crystalline and amorphous structures (Fig. 1e). This inference was also verified by the corresponding fast Fourier transform patterns in selected regions with bright spots (Fig. 1f) and diffusion loops (Fig. 1g).



Scheme 1. Schematic illustration. Schematic illustration of the as-prepared samples synthesis process.

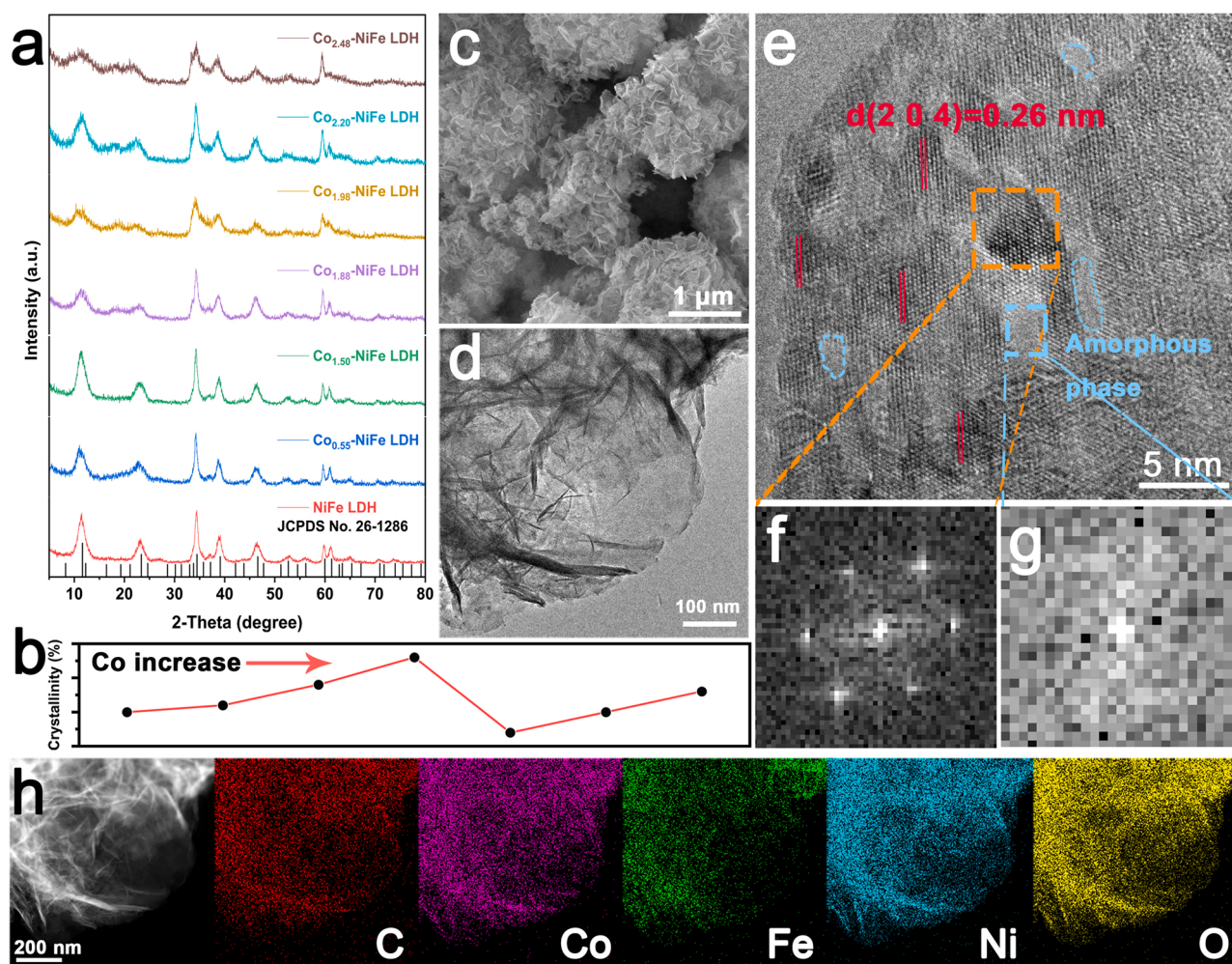


Fig. 1. Physical characterization of catalysts. (a) XRD patterns, and corresponding (b) Crystallinity trend graph of the samples, (c) SEM image of Co_{1.98}-NiFe LDH loading on the carbon fiber paper, (d) TEM image, (e) high-resolution TEM image, (f, g) the corresponding FFT patterns of the selected regions marked by the orange and blue squares, respectively, in (e), and (h) HAADF-STEM image and the corresponding energy-dispersive X-ray spectroscopy elemental maps of Co_{1.98}-NiFe LDH sample.

The selected area electron diffraction (SAED) pattern indicates that Co_{1.88}-NiFe LDH has bright diffraction spots and clear diffraction rings, indicating both single crystal and polycrystalline phases (Fig. S3f). In contrast, Co_{1.98}-NiFe LDH has very ambiguous diffraction rings (Fig. S5), further confirming its poor crystallinity. The noticeable drop in selected area electron diffraction from Co_{1.88}-NiFe LDH to Co_{1.98}-NiFe LDH demonstrates that the crystallinity decreased significantly with a small change in the amount of Co injected. The energy dispersive X-ray analysis (Fig. S6-S7) and the corresponding elemental maps (Fig. 1h and Fig. S3g-k) show a homogeneous distribution of elements in the samples.

Further, the surface chemical characteristics of the samples were investigated using XPS. The XPS survey spectra (Fig. S8a) indicate the coexistence of Fe, Ni, C, and O in all as-prepared samples, and Co-NiFe LDHs also containing Co. As illustrated in Fig. S8b, the C 1s spectra were separated into three peaks at 284.8, 286, and 288.6 eV, corresponding to the C—C, O—C—O, and C=O bonds, respectively [31,32]. The O 1s spectra are fitted to three peak positions corresponding to lattice oxygen (O_L) at approximately 529.7 eV [33,34], hydroxyl groups or absorbed H₂O at approximately 531.3 eV, and oxygen vacancies (O_V) at approximately 532.7 eV (Fig. S8c) [35–37]. As can be observed, the concentration of O_V in Co_{1.98}-NiFe LDH is particularly high. The increase in the O_V might be attributed to the severely deformed local structure generated by the substitution of Ni with Co. As shown in Fig. S9a, the broad Fe 2p_{3/2} envelope is decomposed into a peak centered at ~708 eV and a

prominent peak centered at ~711.5 eV assigned to the Fe²⁺ and Fe³⁺ states, respectively, and a peak at ~714.4 eV corresponding to the satellite peak of Fe²⁺ [34,38,39]. Fig. S9a also shows that as the Co concentration increases, the Fe valence state moves toward a lower binding energy, implying that the increased Co provides more electrons for Fe. Two spin-orbit peaks at ~856.3, and ~858.5 eV corresponding to Ni²⁺, Ni³⁺, and two satellite peaks (denoted by “Sat.”) can be matched to the Ni 2p_{3/2} spectra (Fig. S9b) [40–42]. The Co 2p_{3/2} spectra also fit as two spin-orbit peaks and two satellite peaks at ~781.3 and ~783.9 eV, ~787.2 eV, and ~790 eV corresponding to Co³⁺ and Co²⁺, respectively (Fig. S9c) [43–47].

The O_V/O_L ratio can be used as a yardstick to determine the relative number of surface oxygen vacancies; a higher ratio indicates a greater number of surface oxygen vacancies [33,48]. As shown in Fig. S10 and Table S3, the pattern in the variation of oxygen vacancy is consistent with the change in crystallinity as described above, and the increase in O_V is due to the increase in c-a interface sites. Furthermore, the Ni²⁺/Ni³⁺, Fe²⁺/Fe³⁺, and Co²⁺/Co³⁺ ratios initially declined and subsequently increased in-line with an increase in the oxygen vacancy. This mechanism explains the formation of O_V and the increase in concentration because each oxygen vacancy discharges two electrons, and the free electrons are easily attracted to nearby cations, thereby lowering the energy of the metal ion. Because of the similarity in chemical structure of Co with Ni, XPS analysis shows that the

incorporation of Co had no significant effect on the chemical characteristics and presence of other elements in the sample, but it did create more O_V , which is consistent with the crystallinity analysis.

3.2. OER performances of catalysts

The prepared catalysts were first evaluated for their OER activity in a 1.0 M KOH freshwater electrolyte, with commercial RuO_2 as a comparison benchmark to determine the electrocatalytic behavior. Unless stated otherwise, the potential values presented in this study were iR-corrected and referenced to the RHE. Fig. 2a shows the LSV polarization curves of the catalysts recorded after CV stabilization. In the presence of Co, the characteristic Ni oxidation peak (1.45 V for pristine NiFe LDH) is advanced to 1.4 V (Fig. S11), which indicates that the Co-NiFe LDHs are prone to change to a more catalytically active NiOOH phase with a higher oxidation state ($\geq 3^+$) than the pristine NiFe LDH [49,50]. The $Co_{1.98}$ -NiFe LDH exhibits the lowest overpotentials (η) of 238 mV, reaching the current density of 20 mA cm^{-2} , compared to the blank CFP (366 mV), NiFe LDH (263 mV), $Co_{0.55}$ -NiFe LDH (257 mV), $Co_{1.50}$ -NiFe LDH (269 mV), $Co_{1.88}$ -NiFe LDH (272 mV), $Co_{2.20}$ -NiFe LDH (250 mV), $Co_{2.48}$ -NiFe LDH (267 mV) as well as commercial RuO_2 (333 mV) (Fig. S12 and Table S4). It is also one of the best ternary transition metal

catalysts compared with other reported OER catalysts (Fig. S13 and Table S5). $Co_{1.98}$ -NiFe LDH also exhibits a smaller Tafel slope of 52 mV dec^{-1} , suggesting that the rate-determining step is the adsorption of the hydroxyl species on the surface oxide active site M ($M + OH^- \rightarrow MOH_{ads} + e^-$) [51]. However, the Tafel slope does not improve with Co doping when compared to 44 mV dec^{-1} for the pristine NiFe LDH; therefore, the improvement in kinetics is not responsible for optimizing the material performance (Fig. 2b).

The EIS was used to examine the electrical conductivity of the samples. The obtained data were fitted by employing an equivalent circuit consisting of a solution resistance (R_s) in series with two parallel resistors (R_{por} , R_{ct}) and constant-phase elements (CPE_1 and CPE_2). R_{por} is most likely linked to the resistance of the solution in the pores, and R_{ct} - CPE_2 represents the charge-transfer process at the catalyst/electrolyte interface. The obtained values of R_s , R_{por} , and R_{ct} are listed in Table S4. In Fig. 2c, it is seen that the $Co_{1.98}$ -NiFe LDH catalyst exhibited the smallest semicircle associated with the charge-transfer resistance ($R_{por} + R_{ct}$), with the best conductivity and fast interfacial Faradaic reaction process. Further, the variation pattern of $R_{por} + R_{ct}$ is consistent with the variation law of overpotential. Thus, the interfacial resistance is the main factor for improving the electrocatalytic performance. The electrochemically effective surface area (ECSA) is an indication of the

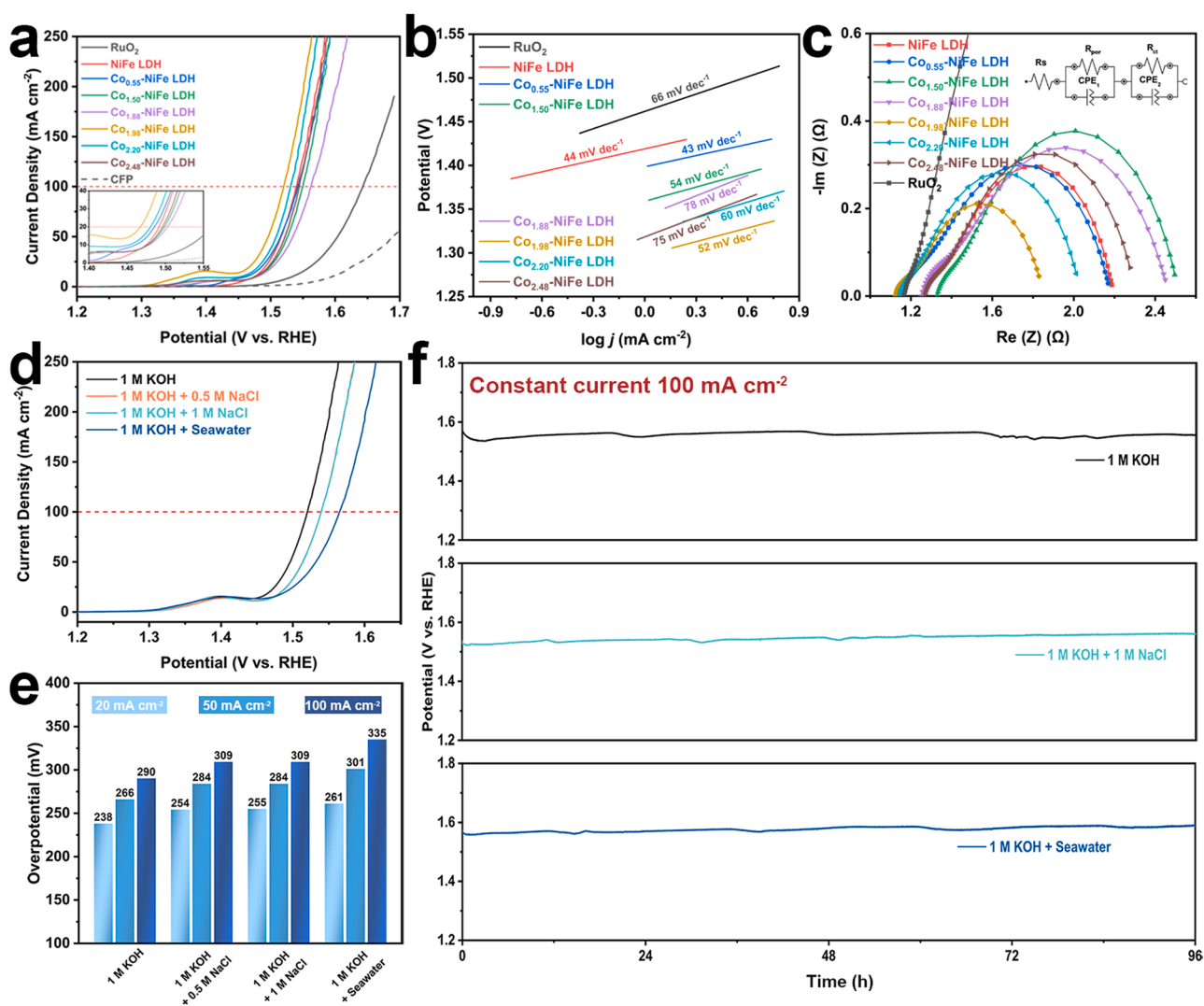


Fig. 2. OER performance of catalysts. (a) iR-corrected LSV curves (inset is in a slight current density range), (b) corresponding Tafel plots, (c) Nyquist plots at an overpotential of 300 mV of NiFe LDH, Co-NiFe LDHs, and commercial RuO_2 loading on the carbon fiber paper in 1.0 M KOH (inset is equivalent circuit diagram), (d) LSV curves and (e) comparison of the overpotentials required to achieve current densities of 20, 50, 100 mA cm^{-2} for the $Co_{1.98}$ -NiFe LDH electrode tested in different electrolytes, (f) long-term stability tests at a constant current density of 100 mA cm^{-2} for $Co_{1.98}$ -NiFe LDH sample in different electrolytes.

intrinsic electrocatalytic activity obtained by calculating the double-layer capacitance (C_{dl}) from the CV curves (Fig. S14). It is evident from Fig. S15a–b that the C_{dl} and corresponding ECSA of $\text{Co}_{1.98}\text{-NiFe}$ LDH were relatively high. Simultaneously, the current density was normalized by the ECSA to exclude geometric effects and evaluate the intrinsic catalytic activity of different samples (Fig. S15c). This shows that the intrinsic activity of the $\text{Co}_{1.98}\text{-NiFe}$ LDH is the best, and consistent with the LSV data. Similarly, TOF is linked to intrinsic activity. $\text{Co}_{1.98}\text{-NiFe}$ LDH outperformed NiFe LDH and other Co–NiFe LDH with a TOF of 0.036 s^{-1} at an overpotential of 300 mV (Fig. S16). The static contact angle measurements indicate that the introduction of Co had no effect on the superhydrophobicity of the NiFe LDH nanosheets, but the contact angle changed from 145° to 143° (Fig. S17). The superhydrophobicity of the $\text{Co}_{1.98}\text{-NiFe}$ LDH effectively promoted the OER kinetics, which is essential for the adsorption/desorption of intermediates during the reaction [52].

The OER properties of the samples were then evaluated in alkaline artificial seawater (1.0 M KOH + 0.5 M NaCl and 1.0 M KOH + 1.0 M NaCl) and alkaline natural seawater electrolytes (1.0 M KOH + seawater) (Fig. S18 and Table S6). $\text{Co}_{1.98}\text{-NiFe}$ LDH maintained the best OER activity in 1.0 M KOH + 0.5 M NaCl electrolyte (Fig. 2d), even in high concentration saline, reaching current densities of 20, 50, and 100 mA cm^{-2} with overpotential of only 255, 284, and 309 mV,

respectively (Fig. 2e). Moreover, other catalysts in these salines perform similarly as in 1.0 M KOH (Fig. S19a and S20a). The slight decrease in material activity is mainly due to the increased resistance of the material in the brine (Fig. S19b and Fig. S20b). All the prepared samples exhibited some reduction in activity in 1.0 M KOH + seawater electrolyte (Fig. S21a), which is mainly caused by contaminants in seawater, including bacteria, microorganisms, solid particles, and insoluble solids, formed on the catalyst surface (Fig. S21b). In this case, $\text{Co}_{1.98}\text{-NiFe}$ LDH requires an overpotential of only 261, 301, and 335 mV to reach current densities of 20, 50, and 100 mA cm^{-2} , respectively, which far exceeds that of the benchmark RuO_2 .

Stability is an essential index for evaluating catalyst performance. Therefore, the performance stability of the $\text{Co}_{1.98}\text{-NiFe}$ LDH at high current densities was measured, in different electrolytes. As illustrated in Fig. 2f, the overpotential increased only slightly in the electrolytes operating at a current density of 100 mA cm^{-2} for more than 96 h, proving the excellent stability of the $\text{Co}_{1.98}\text{-NiFe}$ LDH and its corrosion resistance to seawater.

The main reasons for the resistance of this catalyst to chlorine in seawater include the following reasons. First, the $\text{Co}_{1.98}\text{-NiFe}$ LDH is superhydrophobic (Fig. S17b), which can substantially reduce the contact with chlorine ions and pollutants in saline electrolytes on the basis of maintaining normal OER reaction, and fundamentally reduce the

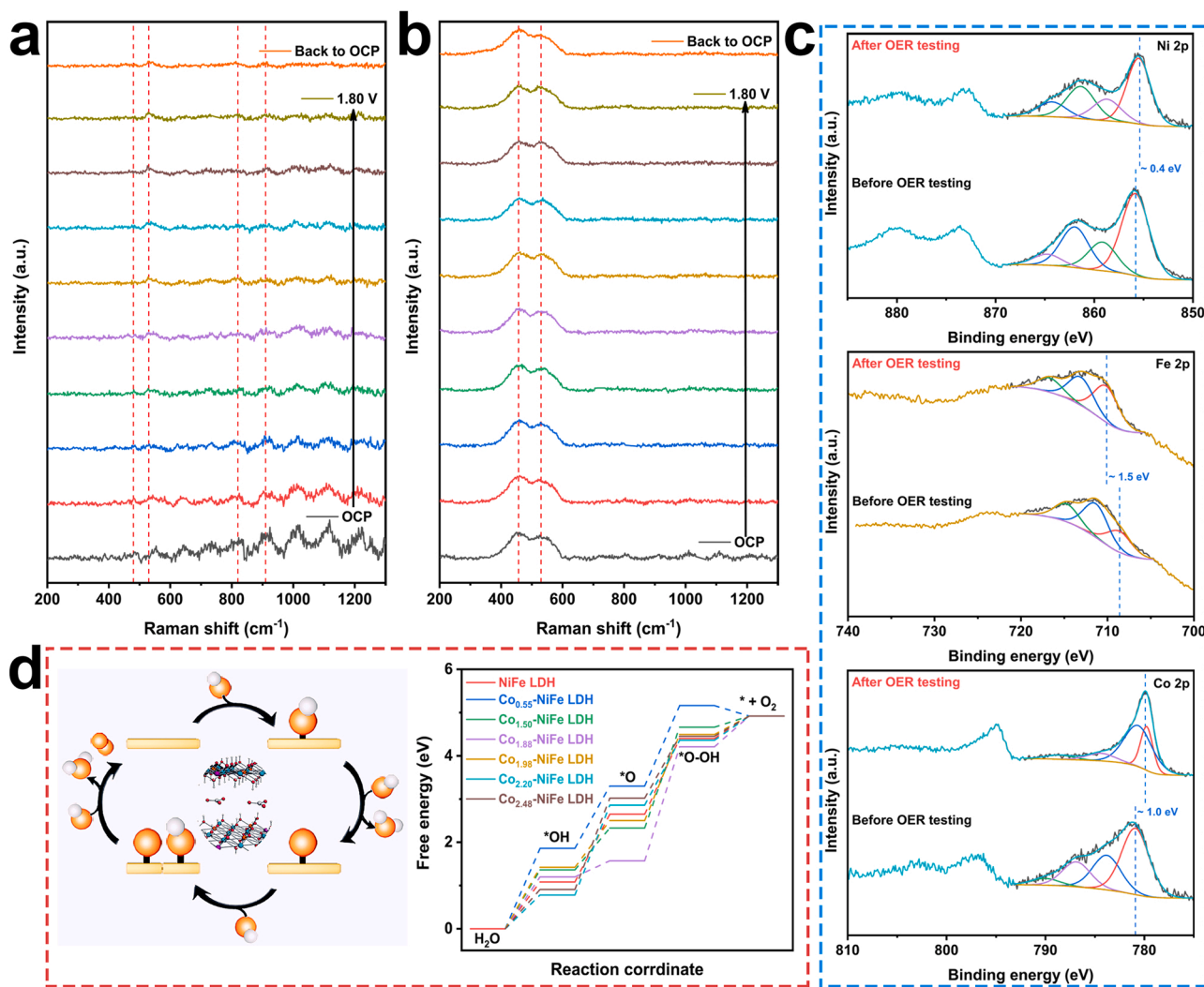


Fig. 3. Mechanism investigation of $\text{Co}_{1.98}\text{-NiFe}$ LDH during the OER process. In-situ Raman spectra of (a) NiFe LDH, and (b) $\text{Co}_{1.98}\text{-NiFe}$ LDH measured in 1.0 M KOH at various potentials versus RHE during OER process, (c) Ni 2p, Fe 2p, and Co 2p core-level XPS spectra of $\text{Co}_{1.98}\text{-NiFe}$ LDH before and after the stability test, (d) proposed OER pathway on $\text{Co}_{1.98}\text{-NiFe}$ LDH and free energy diagram for OER on different models.

corrosion; second, the corrosion of the material by seawater is mainly due to the chlorine-containing by-products produced [53]. We monitored the gas composition of the OER reaction by online gas chromatography. A high Faraday efficiency of 97.38% for oxygen was obtained and no chlorine-containing by-products were detected (Fig. S22); third, Co_{1.98}-NiFe LDH has a stable multilayered nanosheet structure, and the following in-situ Raman tests proved that it has the recover property after the reaction (Fig. 3b and S23b). These properties enable the material to be super resistant against chlorine in saline electrolytes.

3.3. Dynamic change of surface and mechanism investigation

The in-situ Raman technique was employed to examine the evolution of NiFe LDH and Co_{1.98}-NiFe LDH in real time to investigate the surface reconstruction phenomenon during the OER reaction. When no voltage was applied, as shown in Fig. 3a, the pristine NiFe LDH exhibited a large number of peaks, with peaks at 480 and 530 cm⁻¹ attributed to the Ni-O bending vibration modes of NiOOH [54,55], and peaks at 640 and 730 cm⁻¹ stretches, indicating the presence of interlayer Fe ions [56, 57]. The transition metal-bound hydroperoxide ligands range from 820 to 1120 cm⁻¹ [58–64], and the peak at 1220 cm⁻¹ corresponds to C-H bending produced by carbon fiber paper [65,66]. With increasing voltage, the intensity at 530 cm⁻¹ steadily increased indicating the creation of additional NiOOH during the OER reaction [67].

In contrast, Co_{1.98}-NiFe LDH first exhibits relatively fewer peaks; the peak at 457 cm⁻¹ corresponds to the vibration of Ni^{II}-O in crystalline Ni(OH)₂, and that at 530 cm⁻¹ corresponds to Ni^{II}-O in disordered or defective Ni(OH)₂, with the broadening of the peak indicating a decrease in crystallinity (Fig. 3b). In particular, the intensity of the peak at 530 cm⁻¹ for Co_{1.98}-NiFe LDH gradually equaled the intensity of that at 457 cm⁻¹, as the voltage increased, from less than 457 cm⁻¹ at OCP. When the voltage was reduced from 1.8 V to OCP, the NiFe LDH remained in the NiOOH phase, whereas the peak at 530 cm⁻¹ for the Co_{1.98}-NiFe LDH returned to its starting state (Fig. S23). This phenomenon proves the excellent stability of the Co_{1.98}-NiFe LDH. These variations suggest that the numerous c-a structures created by Co doping, thereby effectively accelerating the transfer from M-OH to M-OOH at the surface sites while stabilizing the material structure; this allows the catalyst to operate efficiently and reliably at high voltage for an extended period.

In the OER process, the lattice-oxygen-mediated mechanism (LOM) was found to exhibit pH-dependent OER kinetics on the RHE scale [68]. Therefore, we performed pH-dependent experiments for RuO₂, NiFe LDH, and Co_{1.98}-NiFe LDH to investigate this mechanism. Different behaviors were exhibited, with RuO₂ showing pH-independent kinetic behavior, typical of the adsorbate evolution mechanism, while NiFe LDH and Co_{1.98}-NiFe LDH exhibited a distinct pH dependence, suggesting LOM mechanism (Fig. S24). The structures of the samples after long-term stability testing were further investigated using XPS. The element F derived from the binder (Nafion solution) added during ink making (Fig. S25a). The activation of lattice oxygen is often associated with instability owing to the escape of internal lattice oxygen, as previously reported for LOM [69]. The O 1 s plot (Fig. S25b) revealed the presence of lattice oxygen (O_L), hydroxide groups, and oxygen vacancies (O_V). As previously stated in the discussion of XPS results, O_V/O_L can show the magnitude of oxygen vacancy concentration, and the ratio of O_V/O_L before and after the test is 1.92 and 1.37, respectively, indicating no increase in oxygen defect concentration [49], indicating superior material stability. From the Ni 2p, Fe 2p, and Co 2p patterns (Fig. 3c), the binding energy of Ni is negatively shifted by about 0.4 eV, indicating more Ni(OH)₂ formation, which is consistent with the above Raman results. In contrast, the overall shift of Fe and Co to higher valence states is beneficial to the OER performance. The contact angle of Co_{1.98}-NiFe LDH, which remained superhydrophobicity, was also measured before and after the stability test (Fig. S26). More directly, the SEM, XRD, and TEM images of Co_{1.98}-NiFe LDH were examined before and after the

long-term stability test in 1.0 M KOH. The SEM images proved that the morphology of the material nanosheets remained after a long testing period. However, the nanosheets agglomerated, obscuring some of the active sites, which could explain the slightly reduced performance (Fig. S27). After the durability test, the XRD and TEM data demonstrated that the phase and crystalline structure remained intact, indicating that no unique structural rebuilding was generated by oxidation through the activated lattice oxygen (Fig. S28). These findings support the high stability of the Co_{1.98}-NiFe LDH.

To elucidate the excellent OER activity and stability of the Co_{1.98}-NiFe LDH and the LOM mechanism of local activation, density functional theory calculations were performed. Fig. 3d (left column) shows the optimized OER pathway on the material surface. The Gibbs free energy diagram indicates that the rate-determining step of OER changes with increasing Co content. The rate-determining step for NiFe LDH changed from the formation of the *O-OH intermediate to the formation of the *O intermediate in Co_{2.20}-NiFe LDH and Co_{2.48}-NiFe LDH (Fig. 3d, right column). The corresponding overpotentials are shown in Fig. S29, which similar from the actual experimental results except for the pristine NiFe LDH. This different point is primarily because the theoretical calculations do not consider the effect of crystallinity caused from Co doping, where a large number of c-a interfaces would provide a large number of active sites and affect the electron transfer.

3.4. Performance as an anode in water-splitting and seawater-splitting

Encouraged by the excellent OER performance and stability of the Co_{1.98}-NiFe LDH, it was applied in seawater-splitting process. A two-electrode electrolyzer was constructed for seawater splitting in different simulated and natural seawater electrolytes, where Co_{1.98}-NiFe LDH as the anode was coupled with Pt/C as the cathode. Notably, the electrolyzer exhibited excellent overall seawater splitting activity in the two alkaline simulated seawater electrolytes (Fig. 4a). Without iR compensation, only 1.5, 1.66, and 1.82 V was required to reach 10, 50, and 100 mA cm⁻² in 1 M KOH, and even in 1 M KOH + 1 M NaCl, the same current density was achieved with 1.53, 1.67, and 1.84 V, respectively. In the case of natural alkaline seawater (1 M KOH + seawater), the activity was slightly decreased owing to impurities in the seawater, yet it was still significant (Fig. 4b). Simultaneously, the electrolyzers exhibited excellent stability. In 1 M KOH, 1 M KOH + 1 M NaCl, and 1 M KOH + seawater, the test voltage remained highly robust at a current density of 10 mA cm⁻² for over 96 h (Fig. 4c). In conclusion, the electrode materials used in this study, have superior activity and stability, and show great potential for rapid hydrogen production in pure water electrolysis and seawater electrolysis.

In summary, we synthesized a series of Co-NiFe LDHs based on NiFe LDH. In the previously reported doping of heteroatoms, to improve the c-a interfacial active site, an increase in the concentration of heteroatoms was observed, with the crystallinity of the sample gradually decreased, and new substances being generated. In contrast, in the present study, the material composition of the Co-NiFe LDH did not change because the atomic structures of Co and Ni were very similar. In addition, the crystallinity of the sample is not negatively correlated with the heteroatom concentration, as previously reported. Subsequent OER performance tests showed that the trend of the OER activity of the samples was consistent with that of the sample crystallinity. As shown in Fig. 4d, the change in crystallinity caused by the doping of Co regulates the number of c-a interface sites formed which affected the OER activity of the catalyst. However, the theoretical overpotential shows that Co_{1.98}-NiFe LDH has a relatively low theoretical overpotential among all Co-NiFe LDHs, with the exception of the NiFeLDH. Owing to the synergistic effect of these factors, the actual experimental overpotential differed from the theoretical overpotential, and Co_{1.98}-NiFe LDH exhibited the best OER activity.

Based on the above analysis, the enhanced catalytic performance of the Co_{1.98}-NiFe LDH, exhibiting the highest activity among the Co-NiFe

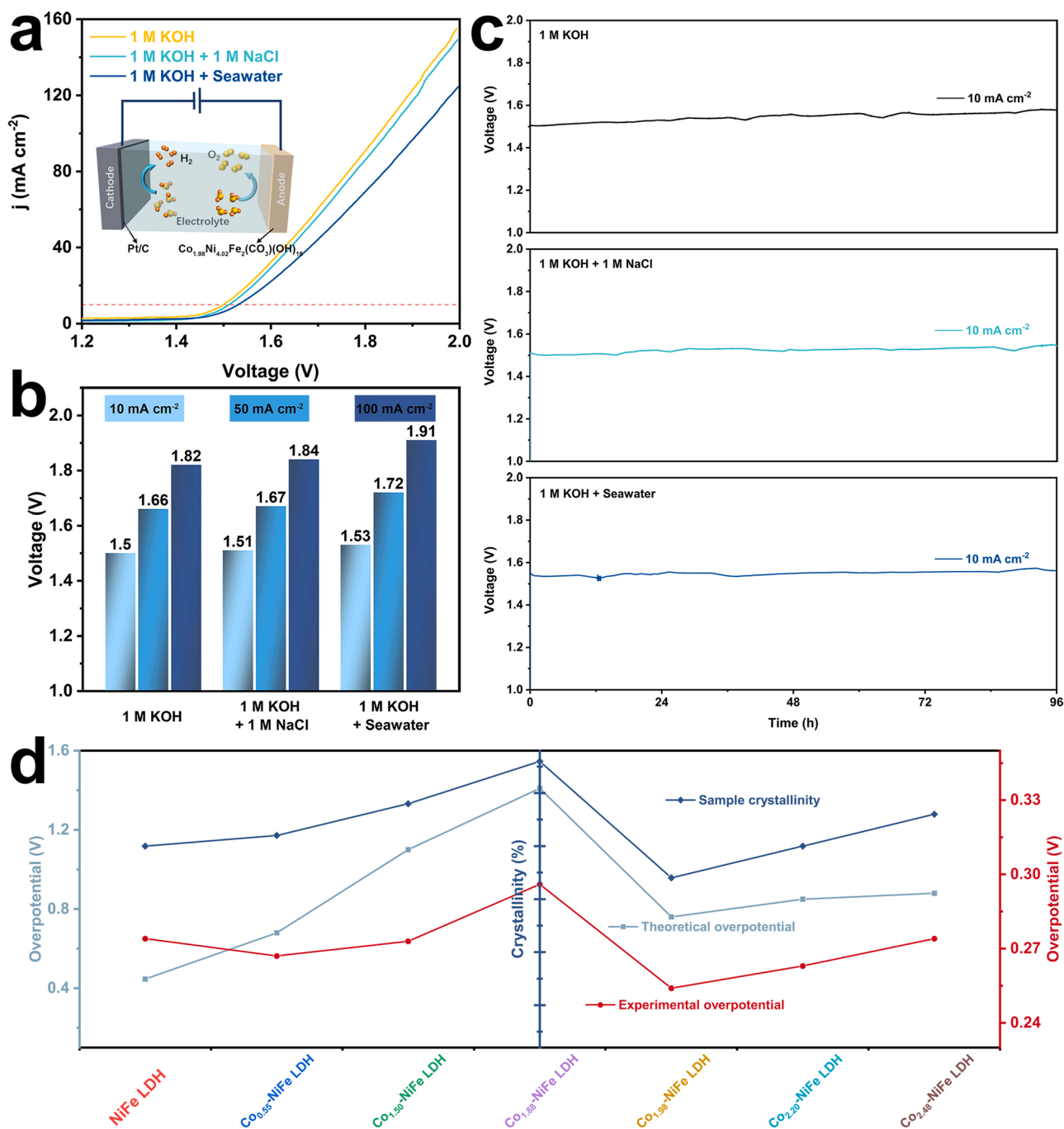


Fig. 4. Overall water-splitting performance. (a) Polarization curves (inset is a schematic illustration of the electrolyzer), (b) comparison of the required voltages at current densities of 10, 50, and 100 mA cm⁻², (c) long-term stability tests at a constant current density of 100 mA cm⁻² for Co_{1.98}-NiFe LDH electrolyzer in different electrolytes and (d) crystallinity, DFT calculated overpotentials and experimental overpotentials of as-prepared catalysts.

LDHs studied, was determined to be caused by the following factors. First, the multilayered ultrathin nanosheet structure facilitated the exposure of active sites and electron transfer; second, the minimum crystallinity enabled increase in c-a active sites and oxygen defects without affecting the stability, which contributed to the enhanced OER activity; and third, density functional theory calculations demonstrated that Co_{1.98}-NiFe LDH has the smallest adsorption energy among various intermediates in a series of Co-NiFe LDH. In addition to testing the properties and performance of the material, we also proposed a method of doping with similar elements. However, there are inevitable limitations, and requirement of in-depth understanding of the changes in the material during synthesis process for the reasons for the changes in

crystallinity. Further, in future, the method should be extended to other families of similar elements and applications.

4. Conclusions

In conclusion, we used Co, which is very similar to Ni, to modulate the crystallinity of NiFe LDH, forming a large number of c-a interfaces while maintaining the stability of the material to the maximum extent. Extensive physical and chemical characterization results proved that the introduction of Co leads to a change in the crystallinity of NiFe LDH, the formation of c-a interfaces, and the regulation of the electronic structure of the material. The OER activity of the samples were also tested. The

Co_{1.98}-NiFe LDH required an overpotential of only 236 mV to reach a current density of 20 mA cm⁻² and exhibited excellent performance in both artificial seawater and natural seawater electrolytes. A two-electrode water-splitting system consisting of Co_{1.98}-NiFe LDH as the anode and commercial Pt/C as the cathode requires only a very low voltage (1.5 V) to reach the current density of 10 mA cm⁻². In-situ Raman spectrum tests also elucidated the changes in the sample surface during OER. Finally, the combination of density functional theory calculations and electrochemical analysis proved that the improvement of the material performance is mainly due to the modulation of the crystallinity of material leading to the increase in the number of c-a interfaces. Unlike the traditional methods of introducing heteroatoms which destroy the crystal structure, this new approach does not destroy the crystal structure or form other substances. This study provides a novel concept for designing more efficient and durable OER catalysts.

CRediT authorship contribution statement

Yang Yang: Conceptualization, Methodology, Validation, Writing – original draft preparation. **Shuya Wei:** Investigation. **Yafei Li:** Investigation. **Donggang Guo:** Writing – review & editing. **Huajie Liu:** Writing – review & editing. **Lu Liu:** Resources, Supervision, Writing – review & editing.

Declaration of Competing Interest

The authors declare that they have no known competing financial interests or personal relationships that could have appeared to influence the work reported in this paper.

Acknowledgment

This work was supported by the Tianjin Science and Technology support key projects (20JCYBJC01420) and the Tianjin science and technology support key projects (18YFZCSF00500). The authors would like to thank Shiyanjia Lab (www.shiyanjia.com) for supporting AFM, XPS, static contact angle, and in situ Raman tests.

Appendix A. Supporting information

Supplementary data associated with this article can be found in the online version at [doi:10.1016/j.apcatb.2022.121491](https://doi.org/10.1016/j.apcatb.2022.121491).

References

- [1] L. Xu, Q. Jiang, Z. Xiao, X. Li, J. Huo, S. Wang, L. Dai, Plasma-engraved Co₃O₄ nanosheets with oxygen vacancies and high surface area for the oxygen evolution reaction, *Angew. Chem., Int. Ed.* 55 (2016) 5277–5281.
- [2] Y. Jiao, Y. Zheng, M. Jaroniec, S.Z. Qiao, Design of electrocatalysts for oxygen- and hydrogen-involving energy conversion reactions, *Chem. Soc. Rev.* 44 (2015) 2060–2086.
- [3] R. Gao, J. Zhu, D. Yan, Transition metal-based layered double hydroxides for photo (electro)chemical water splitting: a mini review, *Nanoscale* 13 (2021) 13593–13603.
- [4] C. Liu, J. Qian, Y. Ye, H. Zhou, C.-J. Sun, C. Sheehan, Z. Zhang, G. Wan, Y.-S. Liu, J. Guo, S. Li, H. Shin, S. Hwang, T.B. Gunnoe, W.A. Goddard, S. Zhang, Oxygen evolution reaction over catalytic single-site Co in a well-defined brookite TiO₂ nanorod surface, *Nat. Catal.* 4 (2021) 36–45.
- [5] S. Li, B. Chen, Y. Wang, M.-Y. Ye, P.A. van Aken, C. Cheng, A. Thomas, Oxygen-evolving catalytic atoms on metal carbides, *Nat. Mater.* 20 (2021) 1240–1247.
- [6] R. Gao, D. Yan, Recent development of ni/fe-based micro/nanostructures toward photo/electrochemical water oxidation, *Adv. Energy Mater.* 10 (2020), 1900954.
- [7] I. Roger, M.A. Shipman, M.D. Symes, Earth-abundant catalysts for electrochemical and photoelectrochemical water splitting, *Nat. Rev. Chem.* 1 (2017) 0003.
- [8] H. Guo, Z. Fang, H. Li, D. Fernandez, G. Henkelman, S.M. Humphrey, G. Yu, Rational design of rhodium–iridium alloy nanoparticles as highly active catalysts for acidic oxygen evolution, *ACS Nano* 13 (2019) 13225–13234.
- [9] D. Chen, C. Chen, Z.M. Baiyee, Z. Shao, F. Ciucci, Nonstoichiometric oxides as low-cost and highly-efficient oxygen reduction/evolution catalysts for low-temperature electrochemical devices, *Chem. Rev.* 115 (2015) 9869–9921.
- [10] T. Reier, M. Oezaslan, P. Strasser, Electrocatalytic oxygen evolution reaction (OER) on Ru, Ir, and Pt catalysts: a comparative study of nanoparticles and bulk materials, *ACS Catal.* 2 (2012) 1765–1772.
- [11] W. Ye, Y. Yang, X. Fang, M. Arif, X. Chen, D. Yan, 2D cocrystallized metal–organic nanosheet array as an efficient and stable bifunctional electrocatalyst for overall water splitting, *ACS Sustainable Chem. Eng.* 7 (2019) 18085–18092.
- [12] C. Walter, P.W. Menezes, S. Orthmann, J. Schuch, P. Connor, B. Kaiser, M. Lerch, M. Driess, A molecular approach to manganese nitride acting as a high performance electrocatalyst in the oxygen evolution reaction, *Angew. Chem., Int. Ed.* 57 (2018) 698–702.
- [13] M. Arif, G. Yasin, M. Shakeel, M.A. Mushtaq, W. Ye, X. Fang, S. Ji, D. Yan, Highly active sites of NiVB nanoparticles dispersed onto graphene nanosheets towards efficient and pH-universal overall water splitting, *J. Energy Chem.* 58 (2021) 237–246.
- [14] R. Gao, H. Zhang, D. Yan, Iron diselenide nanoplatelets: Stable and efficient water-electrolysis catalysts, *Nano Energy* 31 (2017) 90–95.
- [15] H. Sun, C.-W. Tung, Y. Qiu, W. Zhang, Q. Wang, Z. Li, J. Tang, H.-C. Chen, C. Wang, H.M. Chen, Atomic metal–support interaction enables reconstruction-free dual-site electrocatalyst, *J. Am. Chem. Soc.* (2021).
- [16] Y. Wang, L. Yan, K. Dastafkan, C. Zhao, X. Zhao, Y. Xue, J. Huo, S. Li, Q. Zhai, Lattice matching growth of conductive hierarchical porous MOF/LDH heteronanotube arrays for highly efficient water oxidation, *Adv. Mater.* 33 (2021), 2006351.
- [17] R. Gao, D. Yan, D.G. Evans, X. Duan, Layer-by-layer assembly of long-afterglow self-supporting thin films with dual-stimuli-responsive phosphorescence and antiforgery applications, *Nano Res.* 10 (2017) 3606–3617.
- [18] Y. Li, L. Zhang, X. Xiang, D. Yan, F. Li, Engineering of ZnCo-layered double hydroxide nanowalls toward high-efficiency electrochemical water oxidation, *J. Mater. Chem. A* 2 (2014) 13250–13258.
- [19] L. Yao, N. Zhang, Y. Wang, Y. Ni, D. Yan, C. Hu, Facile formation of 2D Co₂P@Co₃O₄ microspheres through in-situ topotactic conversion and surface corrosion: Bifunctional electrocatalysts towards overall water splitting, *J. Power Sources* 374 (2018) 142–148.
- [20] M. Arif, G. Yasin, L. Luo, W. Ye, M.A. Mushtaq, X. Fang, X. Xiang, S. Ji, D. Yan, Hierarchical hollow nanotubes of NiFeV-layered double hydroxides@CoVP heterostructures towards efficient, pH-universal electrocatalytic nitrogen reduction reaction to ammonia, *Appl. Catal., B: Environ.* 265 (2020), 118559.
- [21] H. Xu, B. Fei, G. Cai, Y. Ha, J. Liu, H. Jia, J. Zhang, M. Liu, R. Wu, Boronization-induced ultrathin 2D nanosheets with abundant crystalline–amorphous phase boundary supported on nickel foam toward efficient water splitting, *Adv. Energy Mater.* 10 (2020), 1902714.
- [22] H. Han, H. Choi, S. Mhin, Y.-R. Hong, K.M. Kim, J. Kwon, G. Ali, K.Y. Chung, M. Je, H.N. Umh, D.-H. Lim, K. Davey, S.-Z. Qiao, U. Paik, T. Song, Advantageous crystalline–amorphous phase boundary for enhanced electrochemical water oxidation, *Energy Environ. Sci.* 12 (2019) 2443–2454.
- [23] Y. Chen, Z. Lai, X. Zhang, Z. Fan, Q. He, C. Tan, H. Zhang, Phase engineering of nanomaterials, *Nat. Rev. Chem.* 4 (2020) 243–256.
- [24] J. Huang, H. Sheng, R.D. Ross, J. Han, X. Wang, B. Song, S. Jin, Modifying redox properties and local bonding of Co₃O₄ by CeO₂ enhances oxygen evolution catalysis in acid, *Nat. Commun.* 12 (2021) 3036.
- [25] J. Wang, M. Zhang, G. Yang, W. Song, W. Zhong, X. Wang, M. Wang, T. Sun, Y. Tang, Heterogeneous bimetallic Mo-NiPx/NiSy as a highly efficient electrocatalyst for robust overall water splitting, *Adv. Funct. Mater.* 31 (2021), 2101532.
- [26] S.A. Chala, M.-C. Tsai, W.-N. Su, K.B. Ibrahim, B. Thirumalraj, T.-S. Chan, J.-F. Lee, H. Dai, B.-J. Hwang, Hierarchical 3D architected Ag nanowires shelled with nimn-layered double hydroxide as an efficient bifunctional oxygen electrocatalyst, *ACS Nano* 14 (2020) 1770–1782.
- [27] X. Yang, P. Deng, D. Liu, S. Zhao, D. Li, H. Wu, Y. Ma, B.Y. Xia, M. Li, C. Xiao, S. Ding, Sulfuration-induced defect and interface tailoring on bismuth oxide for promoting electrocatalytic CO₂ reduction, *J. Mater. Chem. A* 8 (2020) 2472–2480.
- [28] X. Ji, Y. Lin, J. Zeng, Z. Ren, Z. Lin, Y. Mu, Y. Qiu, J. Yu, Graphene/MoS₂/FeCoNi(OH)_x and Graphene/MoS₂/FeCoNiPx multilayer-stacked vertical nanosheets on carbon fibers for highly efficient overall water splitting, *Nat. Commun.* 12 (2021) 1380.
- [29] P. Zhai, Y. Zhang, Y. Wu, J. Gao, B. Zhang, S. Cao, Y. Zhang, Z. Li, L. Sun, J. Hou, Engineering active sites on hierarchical transition bimetal oxides/sulfides heterostructure array enabling robust overall water splitting, *Nat. Commun.* 11 (2020) 5462.
- [30] L. Kuai, J. Geng, C. Chen, E. Kan, Y. Liu, Q. Wang, B. Geng, A reliable aerosol-spray-assisted approach to produce and optimize amorphous metal oxide catalysts for electrochemical water splitting, *Angew. Chem., Int. Ed.* 53 (2014) 7547–7551.
- [31] N. Wang, Y. Wang, Z. Bai, Z. Fang, X. Zhang, Z. Xu, Y. Ding, X. Xu, Y. Du, S. Dou, G. Yu, High-performance room-temperature sodium–sulfur battery enabled by electrocatalytic sodium polysulfides full conversion, *Energy Environ. Sci.* 13 (2020) 562–570.
- [32] S. Wan, J. Peng, Y. Li, H. Hu, L. Jiang, Q. Cheng, Use of synergistic interactions to fabricate strong, tough, and conductive artificial nacre based on graphene oxide and chitosan, *ACS Nano* 9 (2015) 9830–9836.
- [33] Z. Wang, W. Wang, L. Zhang, D. Jiang, Surface oxygen vacancies on Co₃O₄ mediated catalytic formaldehyde oxidation at room temperature, *Catal. Sci. Technol.* 6 (2016) 3845–3853.
- [34] X. Sun, P. Wei, S. Gu, J. Zhang, Z. Jiang, J. Wan, Z. Chen, L. Huang, Y. Xu, C. Fang, Q. Li, J. Han, Y. Huang, Atomic-level Fe–N–C coupled with Fe₃C–Fe nanocomposites

- in carbon matrixes as high-efficiency bifunctional oxygen catalysts, *Small* 16 (2020), 1906057.
- [35] Y. Tang, Q. Liu, L. Dong, H.B. Wu, X.-Y. Yu, Activating the hydrogen evolution and overall water splitting performance of NiFe LDH by cation doping and plasma reduction, *Appl. Catal., B: Environ.* 266 (2020), 118627.
- [36] L. Li, X. Feng, Y. Nie, S. Chen, F. Shi, K. Xiong, W. Ding, X. Qi, J. Hu, Z. Wei, L.-J. Wan, M. Xia, Insight into the effect of oxygen vacancy concentration on the catalytic performance of MnO_2 , *ACS Catal.* 5 (2015) 4825–4832.
- [37] B. Tang, J. Yang, Z. Kou, L. Xu, H.L. Seng, Y. Xie, A.D. Handoko, X. Liu, Z.W. Seh, H. Kawai, H. Gong, W. Yang, Surface-engineered cobalt oxide nanowires as multifunctional electrocatalysts for efficient Zn-Air batteries-driven overall water splitting, *Energy Stor. Mater.* 23 (2019) 1–7.
- [38] H. Ma, M.A. Mahadik, J.W. Park, M. Kumar, H.S. Chung, W.S. Chae, G.W. Kong, H. H. Lee, S.H. Choi, J.S. Jang, Highly self-diffused Sn doping in $\alpha\text{-Fe}_2\text{O}_3$ nanorod photoanodes initiated from $\beta\text{-FeOOH}$ nanorod/FTO by hydrogen treatment for solar water oxidation, *Nanoscale* 10 (2018) 22560–22571.
- [39] R. Arrigo, R. Blume, V. Streibel, C. Genovese, A. Roldan, M.E. Schuster, C. Ampelli, S. Perathoner, J.J. Velasco Vélez, M. Hävecker, A. Knop-Gericke, R. Schlögl, G. Centi, Dynamics at polarized carbon dioxide–iron oxyhydroxide interfaces unveil the origin of multicarbon product formation, *ACS Catal.* 12 (2022) 411–430.
- [40] X.X. Liang, W. Weng, D. Gu, W. Xiao, Nickel based oxide film formed in molten salts for efficient electrocatalytic oxygen evolution, *J. Mater. Chem. A* 7 (2019) 10514–10522.
- [41] L. Zhang, L. Zhuang, H. Liu, L. Zhang, R. Cai, N. Chen, X. Yang, Z. Zhu, D. Yang, X. Yao, Beyond platinum: defects abundant $\text{CoP}_3/\text{Ni}_2\text{P}$ heterostructure for hydrogen evolution electrocatalysis, *Small Science* 1 (2021), 2000027.
- [42] Y.B. Adegbemiga, N. Ullah, M. Xie, S. Hussain, C.J. Oluigbo, W. Yaseen, A. J. Kumar, Y. Xu, J. Xie, Ni_3Fe nanoparticles enclosed by B-doped carbon for efficient bifunctional performances of oxygen and hydrogen evolution reactions, *J. Alloys Compd.* 835 (2020), 155267.
- [43] X. Zhang, X. Li, R. Li, Y. Lu, S. Song, Y. Wang, Highly active core-shell carbon/ NiCo_2O_4 double microtubes for efficient oxygen evolution reaction: ultralow overpotential and superior cycling stability, *Small* 15 (2019), 1903297.
- [44] M. Yu, K.S. Belthle, C. Tüysüz, H. Tüysüz, Selective acid leaching: a simple way to engineer cobalt oxide nanostructures for the electrochemical oxygen evolution reaction, *J. Mater. Chem. A* 7 (2019) 23130–23139.
- [45] Y. Xu, F. Zhang, T. Sheng, T. Ye, D. Yi, Y. Yang, S. Liu, X. Wang, J. Yao, Clarifying the controversial catalytic active sites of Co_3O_4 for the oxygen evolution reaction, *J. Mater. Chem. A* 7 (2019) 23191–23198.
- [46] S. Liu, H. Cheng, K. Xu, H. Ding, J. Zhou, B. Liu, W. Chu, C. Wu, Y. Xie, Dual modulation via electrochemical reduction activation on electrocatalysts for enhanced oxygen evolution reaction, *ACS Energy Lett.* 4 (2019) 423–429.
- [47] N.K. Oh, C. Kim, J. Lee, O. Kwon, Y. Choi, G.Y. Jung, H.Y. Lim, S.K. Kwak, G. Kim, H. Park, In-situ local phase-transitioned MoSe_2 in $\text{La}_{0.5}\text{Sr}_{0.5}\text{CoO}_3$ -delta heterostructure and stable overall water electrolysis over 1000 h, *Nat Commun* 10 (2019) 1723.
- [48] D.A. Kuznetsov, M.A. Naeem, P.V. Kumar, P.M. Abdala, A. Fedorov, C.R. Müller, Tailoring lattice oxygen binding in ruthenium pyrochlores to enhance oxygen evolution activity, *J. Am. Chem. Soc.* 142 (2020) 7883–7888.
- [49] V. Srinivasan, J.W. Weidner, An electrochemical route for making porous nickel oxide electrochemical capacitors, *J. Electrochem. Soc.* 144 (1997) L210–L213.
- [50] M.-S. Wu, H.-H. Hsieh, Nickel oxide/hydroxide nanoplatelets synthesized by chemical precipitation for electrochemical capacitors, *Electrochim. Acta* 53 (2008) 3427–3435.
- [51] B.M. Jović, U.Č. Lačnjevac, V.D. Jović, N.V. Krstajić, Kinetics of the oxygen evolution reaction on NiSn electrodes in alkaline solutions, *J. Electroanal. Chem.* 754 (2015) 100–108.
- [52] W. Xu, Z. Lu, X. Sun, L. Jiang, X. Duan, Superwetting electrodes for gas-involving electrocatalysis, *Acc. Chem. Res.* 51 (2018) 1590–1598.
- [53] W. Tong, M. Forster, F. Dionigi, S. Dresp, R. Sadeghi Erami, P. Strasser, A.J. Cowan, P. Farràs, Electrolysis of low-grade and saline surface water, *Nat. Energy* 5 (2020) 367–377.
- [54] M.W. Louie, A.T. Bell, An investigation of thin-film Ni-Fe oxide catalysts for the electrochemical evolution of oxygen, *J. Am. Chem. Soc.* 135 (2013) 12329–12337.
- [55] J. Huang, Y. Li, Y. Zhang, G. Rao, C. Wu, Y. Hu, X. Wang, R. Lu, Y. Li, J. Xiong, Identification of key reversible intermediates in self-reconstructed nickel-based hybrid electrocatalysts for oxygen evolution, *Angew. Chem., Int. Ed.* 58 (2019) 17458–17464.
- [56] C. Julien, M. Massot, R. Baddour-Hadjean, S. Franger, S. Bach, J.P. Pereira-Ramos, Raman spectra of birnessite manganese dioxides, *Solid State Ionics* 159 (2003) 345–356.
- [57] F. Zhao, B. Wen, W. Niu, Z. Chen, C. Yan, A. Selloni, C.G. Tully, X. Yang, B.E. Koel, Increasing iridium oxide activity for the oxygen evolution reaction with hafnium modification, *J. Am. Chem. Soc.* 143 (2021) 15616–15623.
- [58] N. Lehnert, F. Neese, R.Y.N. Ho, L. Que, E.I. Solomon, Electronic structure and reactivity of low-spin Fe(III)–hydroperoxo complexes: comparison to activated bleomycin, *J. Am. Chem. Soc.* 124 (2002) 10810–10822.
- [59] F. Neese, J.M. Zaleski, K. Loeb Zaleski, E.I. Solomon, Electronic structure of activated bleomycin: oxygen intermediates in heme versus non-heme iron, *J. Am. Chem. Soc.* 122 (2000) 11703–11724.
- [60] R.Y.N. Ho, G. Roelfes, B.L. Feringa, L. Que, Raman evidence for a weakened O–O bond in mononuclear low-spin Iron(III)–hydroperoxides, *J. Am. Chem. Soc.* 121 (1999) 264–265.
- [61] G. Roelfes, M. Lubben, K. Chen, R.Y.N. Ho, A. Meetsma, S. Genseberger, R. M. Hermant, R. Hage, S.K. Mandal, V.G. Young, Y. Zang, H. Kooijman, A.L. Spek, L. Que, B.L. Feringa, Iron chemistry of a pentadentate ligand that generates a metastable Fe(III)–OOH intermediate, *Inorg. Chem.* 38 (1999) 1929–1936.
- [62] P. Chen, K. Fujisawa, E.I. Solomon, Spectroscopic and theoretical studies of mononuclear copper(II) Alkyl- and hydroperoxo complexes: electronic structure contributions to reactivity, *J. Am. Chem. Soc.* 122 (2000) 10177–10193.
- [63] T.C. Brunold, E.I. Solomon, Reversible dioxygen binding to hemerythrin. 1. electronic structures of deoxy- and oxyhemerythrin, *J. Am. Chem. Soc.* 121 (1999) 8277–8287.
- [64] N. Lehnert, R.Y.N. Ho, L. Que, E.I. Solomon, Spectroscopic properties and electronic structure of low-spin Fe(III)–alkylperoxo complexes: homolytic cleavage of the O–O Bond, *J. Am. Chem. Soc.* 123 (2001) 8271–8290.
- [65] S. Shen, C.-d. Zhu, X.-y. Guo, C.-c. Li, Y. Wen, H.-F. Yang, The synergistic mechanism of phytic acid monolayers and iodide ions for inhibition of copper corrosion in acidic media, *RSC Adv.* 4 (2014) 10597–10606.
- [66] S. Shen, X.-y. Guo, P. Song, Y.-C. Pan, H.-q. Wang, Y. Wen, H.-F. Yang, Phytic acid adsorption on the copper surface: observation of electrochemistry and Raman spectroscopy, *Appl. Surf. Sci.* 276 (2013) 167–173.
- [67] K. Zhu, X. Zhu, W. Yang, Application of in situ techniques for the characterization of nife-based oxygen evolution reaction (OER) electrocatalysts, *Angew. Chem., Int. Ed.* 58 (2019) 1252–1265.
- [68] A. Grimaud, O. Diaz-Morales, B. Han, W.T. Hong, Y.-L. Lee, L. Giordano, K. A. Stoerzinger, M.T.M. Koper, Y. Shao-Horn, Activating lattice oxygen redox reactions in metal oxides to catalyze oxygen evolution, *Nature Chem.* 9 (2017) 457–465.
- [69] T. Reier, Z. Pawolek, S. Cherevko, M. Bruns, T. Jones, D. Teschner, S. Selve, A. Bergmann, H.N. Nong, R. Schlögl, K.J.J. Mayrhofer, P. Strasser, Molecular insight in structure and activity of highly efficient, Low-Ir Ir–Ni oxide catalysts for electrochemical water splitting (OER), *J. Am. Chem. Soc.* 137 (2015) 13031–13040.